




Facile synthesis of CoNi_2S_4 nanoparticles grown on carbon fiber cloth for supercapacitor application

Peng Liu¹ · Yanwei Sui¹ · Fuxiang Wei¹ · Jiqui Qi¹ · Qingkun Meng¹ · Yaojian Ren¹ · Yezeng He^{1,2} 

Received: 24 July 2019 / Accepted: 30 September 2019 / Published online: 5 October 2019
© Springer Science+Business Media, LLC, part of Springer Nature 2019

Abstract

A facile one-step hydrothermal route has been developed to directly synthesize CoNi_2S_4 nanoparticles on carbon fiber cloth (CC) to study the synergistic effect of bimetallic sulfides and carbon substrate on the electrochemical performance of supercapacitor electrode. The integrated binder-free $\text{CoNi}_2\text{S}_4/\text{CC}$ electrode possesses an outstanding specific capacitance of 1165 F g^{-1} at 1 A g^{-1} , and excellent rate capacitance (75.3% retention at 10 A g^{-1}) in a three-electrode system, which is 27.2% and 32.2% higher than that of pure CoNi_2S_4 electrode. Detailed electrochemical tests and results showed that the surface capacitance effect ratio of the $\text{CoNi}_2\text{S}_4/\text{CC}$ electrode is higher than that of pure CoNi_2S_4 electrode because of the introduction of CC. The CC substrates can provide a channel for electrolyte electrons and ions to promote reaction kinetics and shorten the diffusion distance of the redox reaction, thereby improving the performance of the pseudocapacitor CoNi_2S_4 . Besides, the assembled asymmetric supercapacitors based on $\text{CoNi}_2\text{S}_4/\text{CC}$ electrode and reduced graphene oxide electrode displayed a high specific energy density of 33.2 Wh kg^{-1} at 800 W kg^{-1} , remarkable electrochemical stability (87.1% retention after 10,000 circulations) and high rate stability.

1 Introduction

In recent years, with the continuous development of society, new electrochemical energy storage and conversion devices such as supercapacitors, fuel cells and lithium-ion batteries have received extensive attention [1]. Compared with other energy storage and conversion devices, supercapacitors possess the advantages of light weight, fast charging speed, high power density, longer lifespans, environmental friendliness, low preparation cost and so on [2]. They have attracted extensive attention of researchers all over the world. Based on the energy storage mechanisms of supercapacitors, they can be categorized into three types: electric double-layer capacitors (EDLCs), hybrid supercapacitors, and pseudocapacitors [3, 4]. The capacitance of a EDLC is the static electricity generated by the separation at the interface of

electrodes and electrolyte [4, 5]. The capacitance of a hybrid supercapacitor is stemmed from its two electrodes through battery reaction and double layer of electricity, respectively [4]. The capacitance of the pseudocapacitor is derived from the rapid reversible redox reaction of the near surface of the redox active material [4]. The electrodes of EDLCs are mainly composed of carbon materials, and the electrode materials of pseudocapacitors are mainly composed of conductive polymers, transition metal sulfides and transition metal oxides/hydroxides. Compared with EDLCs, pseudocapacitors have attracted widespread attention because of their superior specific capacity [4]. Aqueous electrolytes usually have high conductivity and lower internal resistance of the capacitor [6–9]. Aqueous electrolytes have a small molecular diameter and are easily impregnated with micropores. H_2SO_4 aqueous solution is the most commonly used in acidic aqueous solution, because it has the advantages of high conductivity, ion concentration and low internal resistance. But H_2SO_4 aqueous solution as electrolyte, corrosive, fluid collection can not be used metal materials [7]. Neutral electrolyte has certain advantages in safety performance, but it is aqueous solution electrolyte after all, which is greatly affected by the decomposition voltage of water [7, 8]. For alkaline electrolytes, KOH aqueous solution is most commonly used. Among them, high concentration

✉ Yezeng He
hyz0217@hotmail.com

¹ School of Materials Science and Engineering, China University of Mining and Technology, Xuzhou 221116, People's Republic of China

² The Jiangsu Province Engineering Laboratory of High Efficient Energy Storage Technology and Equipment, Xuzhou, People's Republic of China

KOH electrolyte is used when carbon material is used as electrode material of capacitor, and low concentration KOH electrolyte is used when metal oxide is used as electrode material of capacitor [9].

In recent years, some transition–metal compound, particularly binary nickel–cobalt sulfides (NiCo_2S_4 and CoNi_2S_4), have been widespread researched as promising pseudo-capacitor materials [10]. On the one hand, since the electronegativity of S is lower than O, the material has additional structural flexibility after surface vulcanization, which makes the metal sulfide have higher stability; the transition metal sulfide has a smaller band gap, which also will result in higher conductivity [10–12]. On the other hand, binary Ni–Co sulfides (such as NiCo_2S_4 and CoNi_2S_4) exhibit synergistic effects of Co and Ni species due to multivalent transitions, resulting in better specific capacitance [11, 13, 14]. All the characteristics mentioned above provide a good opportunity for the development of next-generation electrode materials. In the last few years, different morphologies of CoNi_2S_4 and NiCo_2S_4 have been successfully synthesized, such as nanoparticles [15], nanoplates [16], mushroom-like [17] nanowires [18], nanotubes [19], cockscomb flower-like [20], lily-like [21], and nanosheet arrays [22, 23]. For example, Yu et al. [24] synthesized $\text{Ni}_x\text{Co}_{3-x}\text{S}_4$ nanoprisms via a method of sacrificial templates and presented high specific capacitance of 895 F g^{-1} at 1 A g^{-1} . Zhu et al. [25] fabricated NiCo_2S_4 hollow microspheres by gas bubble soft template and their electrochemical measurement results demonstrated a high capacitance of 768 F g^{-1} at a current density of 2 A g^{-1} . Gao et al. [26] synthesized the CoNi_2S_4 nanosheets array on nickel foam at constant potential. The results show that the specific capacitance is 1932 F g^{-1} , when the current density is 2 A g^{-1} . Unfortunately, even though the electrochemical performance of CoNi_2S_4 nanosheets is better than that of other materials, its cycling performance is still dissatisfactory [11]. Therefore, because the reaction kinetics of NiCo_2S_4 and CoNi_2S_4 are slow and dependent on Faraday oxidation–reduction reaction, the rate of long-term charge/discharge is low and the stability is poor [10]. A popular approach to solving this problem is to combine conductive materials. Compared with carbon materials, the using of foam nickel to build an integrated independent electrode can shorten the ions diffusion path and improve the utilization of electroactive atoms, so that the electrochemical performance is improved [10]. However, the influence of oxide and hydroxide on the nickel foam, especially under low mass loading, can not be neglected [10, 12]. Under the same conditions, the contribution of carbon materials can be neglected [12]. Compared with foam nickel substrate, the mass ratio of active material attached to carbon fiber cloth substrates is higher, which provides a broad prospect for the replacement of nickel foam for the preparation of integrated electrodes. Ding et al. [27] fabricated hierarchical

$\text{NiCo}_2\text{S}_4@ \text{NiCo}_x\text{S}_y$ nanoarrays on CC. CoNi_2S_4 interconnected nanosheet was also fabricated arrays on conductive carbon fiber cloth to form a independent electrode with good high-speed channels for electron and electrolyte transport by Chen et al. [28]. As an asymmetric supercapacitors (ASC) electrode, it has good electrochemical performance. Hao et al. [29] prepared hollow NiCo_2S_4 nanotubes array on carbon fabrics. This integrated structure enables the active material to have sufficient electrical contact with carbon fibers, thus improving the effective participation in redox reaction.

Up to now, the most researches have focused on the structural design and method improvement, and there are few studies on the effects of CC on surface capacitive processes and diffusion-controlled reaction kinetics. In this work, CoNi_2S_4 nanoparticles immobilized on carbon cloth were prepared by simple one-step hydrothermal route for application. The introduced CC not only prevented the re-crushing of the CoNi_2S_4 nanoparticles, but also enhanced the connection between the CC backbone and CoNi_2S_4 , and built a high-speed channel for electron transfer. When the as-obtained hybrid material is used as positive electrode materials of supercapacitor, it exhibits an remarkable pseudocapacitive performance with an excellent specific capacitance and capacity retention.

2 Experimental

2.1 Materials

All the chemical reagents and solvents used in this experiment belong to analytical grade and have not been further treatment. The CC was pretreated with potassium permanganate and then ultrasonically washed three times with deionized (DI) water and ethyl alcohol for 30 min each time. Cobalt nitrate hexahydrate ($\text{Co}(\text{NO}_3)_2 \cdot 6\text{H}_2\text{O}$), nickel chloride hexahydrate ($\text{NiCl}_2 \cdot 6\text{H}_2\text{O}$), thioacetamide (TAA, CH_3CSNH_2) and urea (CON_2H_4) were purchased from Aladdin (Shanghai, China).

2.2 Synthesis of CoNi_2S_4

The CoNi_2S_4 was prepared according to a facile one-step hydrothermal route for application. Initially, before using it, the carbon fiber cloth (CC) was pretreated with potassium permanganate and ultrasonically washed three times with DI water and ethyl alcohol, respectively. Then, 0.29105 g of $\text{Co}(\text{NO}_3)_2 \cdot 6\text{H}_2\text{O}$, 0.23769 g of $\text{NiCl}_2 \cdot 6\text{H}_2\text{O}$, 0.06006 g of urea and 0.30052 g of TAA were sequentially added to 30 mL DI deionized water. Then the precursor solution was stirred on a magnetic stirrer for half an hour to form a uniform mixed solution. Two pieces of CC ($2 \text{ cm} \times 1 \text{ cm}$) and

the uniform mixed solution were then poured into a 50 mL Teflon-lined autoclave. Finally, the Teflon-lined autoclave was transferred to an oven and kept at 180 °C for 24 h. After naturally cooling down to room temperature, the sample was ultrasonically rinsed with DI water and ethyl alcohol and dried at 70 °C. CoNi₂S₄ sample was afforded, which is denoted as CoNi₂S₄/CC. For comparison, pure CoNi₂S₄ was also synthesized without CC under the same procedure.

2.3 Characterization

The structures of the obtained materials were analyzed by X-ray diffraction (D8 Advance, Bruker, Germany) with Cu K α radiation in the angle range from 10° to 80° at a scan rate of 8° min⁻¹. The chemical state of the fabricated product was performed and analyzed by X-ray photoelectron spectroscopy (XPS, ESCALAB 250Xi) by Al-K α as X-ray source. Morphologies of the fabricated products were performed by scanning electron microscopy (SEM) (Hitachi SU-8000). Transmission electron microscopy (TEM) and high-resolution TEM (HRTEM, Tecnai G2F20) were also used to observe the morphology and structure of the CoNi₂S₄/CC nanostructures.

2.4 Electrochemical measurements

The electrochemical tests of both three-electrode and two-electrode were carried out in 2 M KOH electrolyte at room temperature. The instrument used for electrochemical measurements was the CHI660D electrochemical workstation (Chenhua, China). The platinum electrode, the reference electrode and the working electrode together constitute a three-electrode system. Platinum foil served as counter electrode, saturated calomel electrode (SCE) as reference electrode, and active material as a work electrode. The mass loading of the CoNi₂S₄ materials on CC was approximately 0.9 mg cm⁻². The CoNi₂S₄/CC (1 cm × 2 cm) was used as the working electrode. For the pure CoNi₂S₄ powder without carbon fiber cloth, the working electrode was the mixture of the acetylene black conductive agent, a polyvinylidene fluoride binder and the obtained CoNi₂S₄ powder in a mass ratio of 1:1:8. The current collector was Ni foam (NF). The mass loading of the pure CoNi₂S₄ material on the NF surface was approximately 1.1 mg cm⁻². The contents of electrochemical testing mainly include cyclic voltammograms (CVs), galvanostatic charge/discharges (GCDs) measurement and electrochemical impedance spectra (EIS) measurement. The specific capacitances (C) of the three-electrode system and two-electrode system can be calculated according to discharge time in GCDs using the following equation [4]:

$$C = \frac{I\Delta t}{m\Delta V} \quad (1)$$

in which I (A) represents charge/discharge current, m (g) symbolizes the accurate weight of the active material, Δt (s) stands for the discharge time in GCDs and ΔV (V) stands for the voltage range upon discharging, respectively.

The electrochemical performance of the sample was further evaluated via an two-electrode system. In the case of ASC, the CoNi₂S₄/CC electrode and r-GO electrode were prepared as the positive electrode and the negative electrode, respectively. The CV, GCDs and EIS of the device were measured in 2 M KOH electrolyte solution. In order to balance the charge storage of negative electrode and positive electrode, the charge stored in negative electrode and positive electrode should be approximately equal. The optimal mass ratio can be calculated according to the equation below [4]:

$$\frac{m^+}{m^-} = \frac{c^- \times \Delta V^-}{c^+ \times \Delta V^+} \quad (2)$$

in which m⁺ and m⁻ are the positive mass and negative mass in the two-electrode system, respectively, ΔV^- and ΔV^+ represent the voltage ranges for the negative electrode and the positive electrode, C⁺ is specific capacity of CoNi₂S₄/CC electrode and C⁻ is specific capacity of the r-GO electrode.

The power density (P, W kg⁻¹) and the energy density (E, Wh kg⁻¹) of CoNi₂S₄/CC//r-GO ASC device can be obtained from the equations below [30]:

$$E = \frac{1}{2} \times C \times \Delta V^2 \quad (3)$$

$$P = \frac{E}{\Delta t} \quad (4)$$

in which Δt (s) stands for the discharge time, ΔV (v) represents the voltage range and C (F g⁻¹) symbolizes the specific capacitance of CoNi₂S₄/CC//r-GO ASC device, respectively.

3 Results and discussion

The composition and structure of CoNi₂S₄/CC and CoNi₂S₄ samples have been investigated by XRD patterns, as depicted in Fig. 1. Obviously, it can be seen that both the CoNi₂S₄/CC and the pure CoNi₂S₄ display the same peaks at 16.28°, 26.82°, 31.52°, 38.30°, 47.33°, 50.29° and 55.22°, which can be identified as the (1 1 1), (2 2 0), (3 1 1), (4 0 0), (4 2 2), (5 1 1), and (4 4 0) planes of the CoNi₂S₄ (JCPDS no. 24-0334), respectively [15, 18, 22, 23]. No other impurity peaks can be found on the XRD patterns of the CoNi₂S₄/CC and CoNi₂S₄, respectively. The well-matched XRD peaks of these two samples demonstrate the preservation of the CoNi₂S₄/CC. The broad diffraction peaks of the CoNi₂S₄/CC sample imply the relatively poor crystallinity.

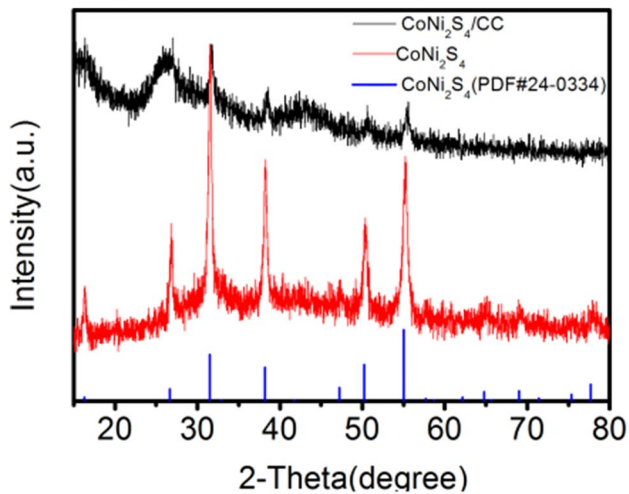


Fig. 1 XRD patterns of the $\text{CoNi}_2\text{S}_4/\text{CC}$ and pure CoNi_2S_4

The element composition and chemical states of the $\text{CoNi}_2\text{S}_4/\text{CC}$ sample were further tested by XPS [11]. The results are shown in Fig. 2a–d. As shown in Fig. 2a, the electrode material is mainly composed of Co, Ni, S and C

element. The C elements may come from the carbon fiber cloth. By Gaussian fitting, the Co 2p and Ni 2p are deconvoluted into multipeaks, including two spin–orbit doublets and two shake-up satellites (Sat) [31, 32]. As displayed in Fig. 2b, the spectrum of Co 2P is matched to two shake-up satellites (Sat) and two spin–orbit doublets ($2P_{3/2}$ and $2P_{1/2}$) [31, 32]. The fitting peaks at 778.5 eV and 793.3 eV are indexed to spin–orbit characteristics of Co^{3+} , while the existing peak located at 781.4 eV and the peak at 797.8 eV correspond to the Co^{2+} ions [33]. In addition, two shake-up satellites can be seen at 802.9 and 783.7 eV [31]. The coexistence of Co^{2+} and Co^{3+} can be determined by spin-energy separation between Co $2p_{1/2}$ and Co $2p_{3/2}$ of about 15 eV. Similarly, the spectrum of Ni 2P can also be matched to two shake-up satellites (sat.) and two spin–orbit doublets ($2P_{3/2}$ and $2P_{1/2}$) [31]. The high-resolution Ni 2p XPS spectrum is shown in Fig. 2c, the binding energies situated at around 853.0 and 870.7 eV corresponded to Ni^{2+} and those at around 855.2 and 873.0 eV indicated Ni^{3+} [31, 32]. S 2p spectrum can also be fitted with one shake-up satellite and two peaks, as shown in Fig. 2d [31]. The binding energies situated located at around 161.7, 162.7 and 168.5 eV are attributed to S $2p_{3/2}$, S $2p_{1/2}$ and the satellite peak,

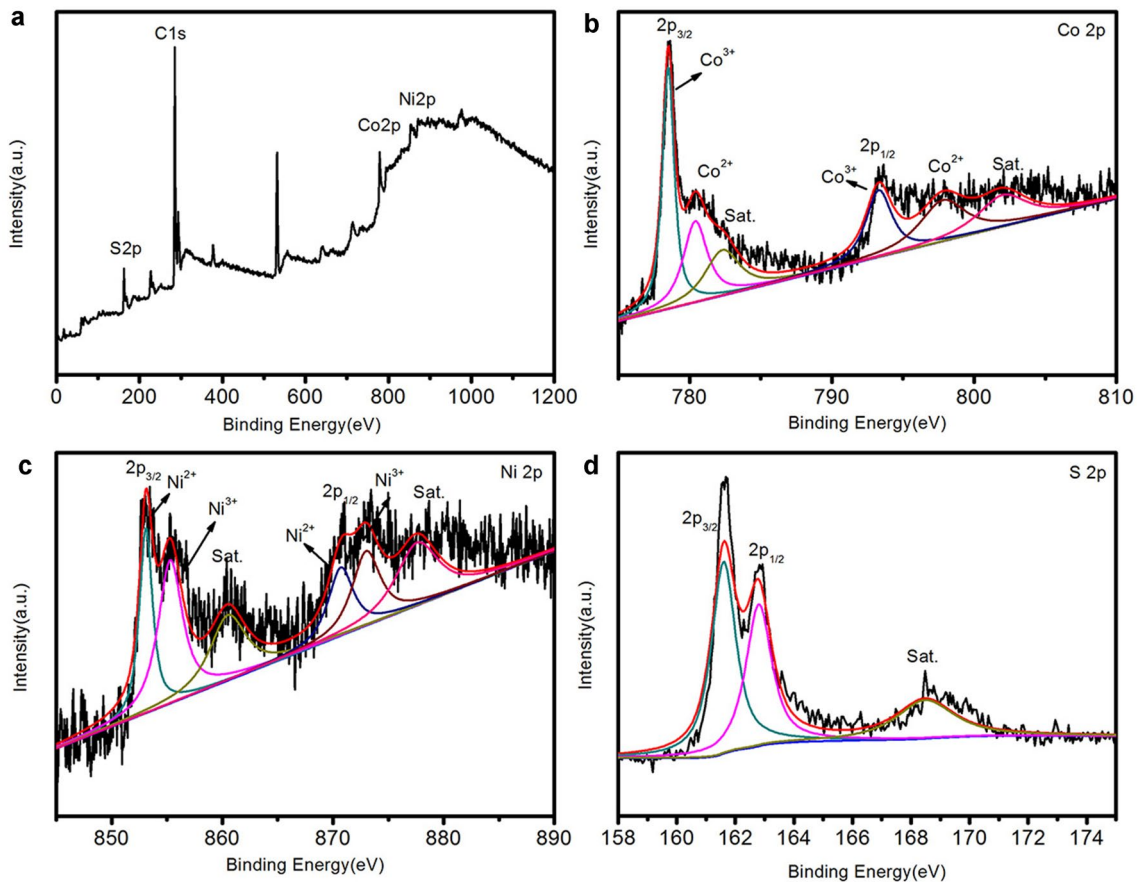


Fig. 2 a XPS survey spectrum of $\text{CoNi}_2\text{S}_4/\text{CC}$; b, d XPS spectra of Co 2p, Ni 2p and S 2p

respectively [31, 32]. According to these XPS results, the $\text{CoNi}_2\text{S}_4/\text{CC}$ material is composed of Co^{3+} , Ni^{3+} , Co^{2+} , Ni^{2+} and S^{2-} , which is consistent with the literature for CoNi_2S_4 [15, 17, 23, 31–36].

The microstructural features of the $\text{CoNi}_2\text{S}_4/\text{CC}$ the $\text{CoNi}_2\text{S}_4/\text{CC}$ hybrid and pure CoNi_2S_4 powder were further investigated by SEM, TEM and HRTEM analysis. Figure 3a shows the bare carbon cloth rough surface and grooves, which is conducive to the deposition of active substances. As shown in Fig. 3b, the carbon fiber cloth is evenly covered by CoNi_2S_4 nanoparticles with an average diameter of approximately 200 nm after hydrothermal reaction. Compared to pure CoNi_2S_4 sample without carbon cloth substrate (Fig. 3c). Compared with pure CoNi_2S_4 powder without CC substrates (Fig. 3c), relatively small nanoparticle diameters and more uniform dispersion in three-electrode and two-electrode systems are critical to accelerating reaction kinetics. The microstructures and the crystallinity of the $\text{CoNi}_2\text{S}_4/\text{CC}$ nanoparticles were further characterized by HRTEM and selected-area electron diffraction (SAED) analysis, which is shown in Fig. 3d. HRTEM image displays the visible lattice fringes with a spacing of 0.2840 nm, which is related to the (311) crystal plane of CoNi_2S_4 and shows no difference with the XRD results. Furthermore, the SAED pattern is depicted in a inset of Fig. 3d. These well-defined diffraction rings can be directed to the (311), (422), (511) and (440) planes of the

CoNi_2S_4 , as marked in Fig. 1, respectively, suggesting the polycrystalline structure of CoNi_2S_4 .

To further research the practicality of the $\text{CoNi}_2\text{S}_4/\text{CC}$ sample as a supercapacitor electrode, its electrochemical performance was investigated by CV, GCDs and EIS measurements in a three-electrode system in 2 M KOH electrolyte. The electrochemical characterizations of the $\text{CoNi}_2\text{S}_4/\text{CC}$ sample and CoNi_2S_4 sample were first performed by CV test with scanning rate of 10–100 mV s^{-1} and the potential window from 0 to 0.7 V. As revealed in Fig. 4a, a couple of well-defined faradaic redox peaks can be observed in the range of 0–0.7 V of the CV curves of the $\text{CoNi}_2\text{S}_4/\text{CC}$ sample, mainly due to the Faraday-type redox reaction [37]. As the increase of scanning rate, the shape of CV keeps very good, which indicated the ideal pseudocapacitance behaviors and excellent rate performance [37, 38]. At the same time, the cathode peaks and anode peaks shift to lower potential and higher potential respectively, which may be caused by an increase of internal resistance and polarization [38]. Figure 4b exhibits a comparison of CV curves of pure CoNi_2S_4 sample and the $\text{CoNi}_2\text{S}_4/\text{CC}$ sample at a scanning rate of 50 mV s^{-1} . Clearly, the $\text{CoNi}_2\text{S}_4/\text{CC}$ material has a larger integral area than the pure CoNi_2S_4 material, that is, the specific capacitances of $\text{CoNi}_2\text{S}_4/\text{CC}$ material are larger. The redox reaction of $\text{CoNi}_2\text{S}_4/\text{CC}$ electrode in KOH electrolyte solution can be expressed by the equation below [39, 40]:

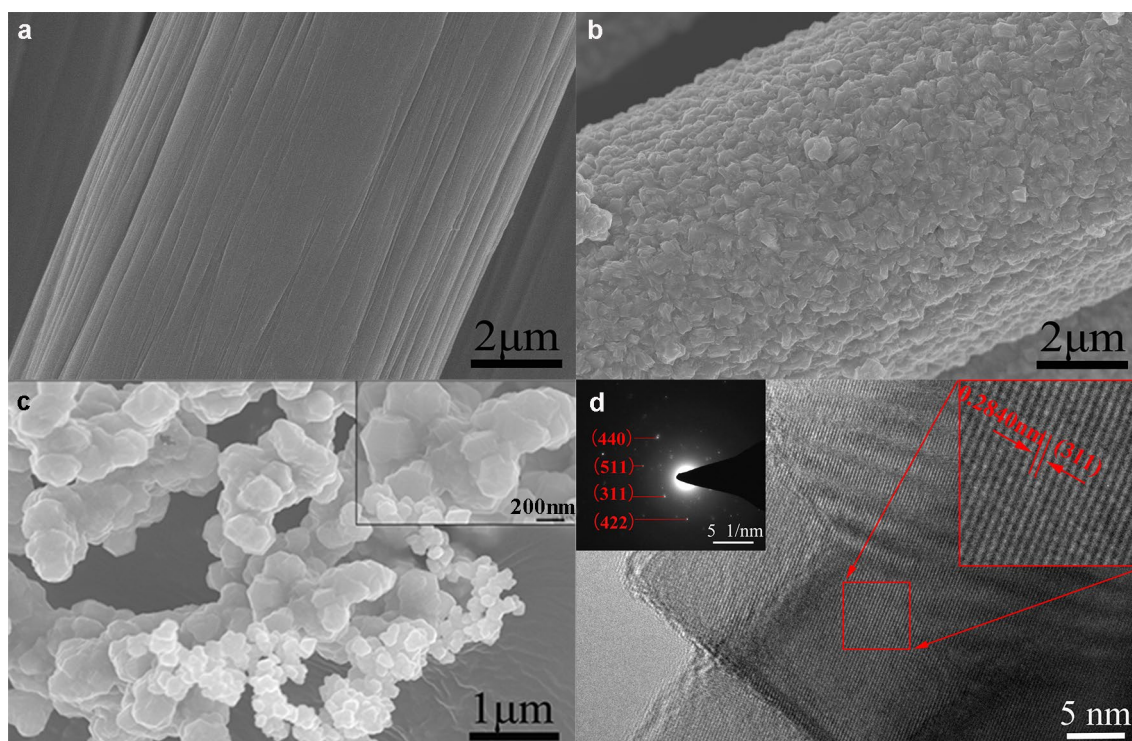
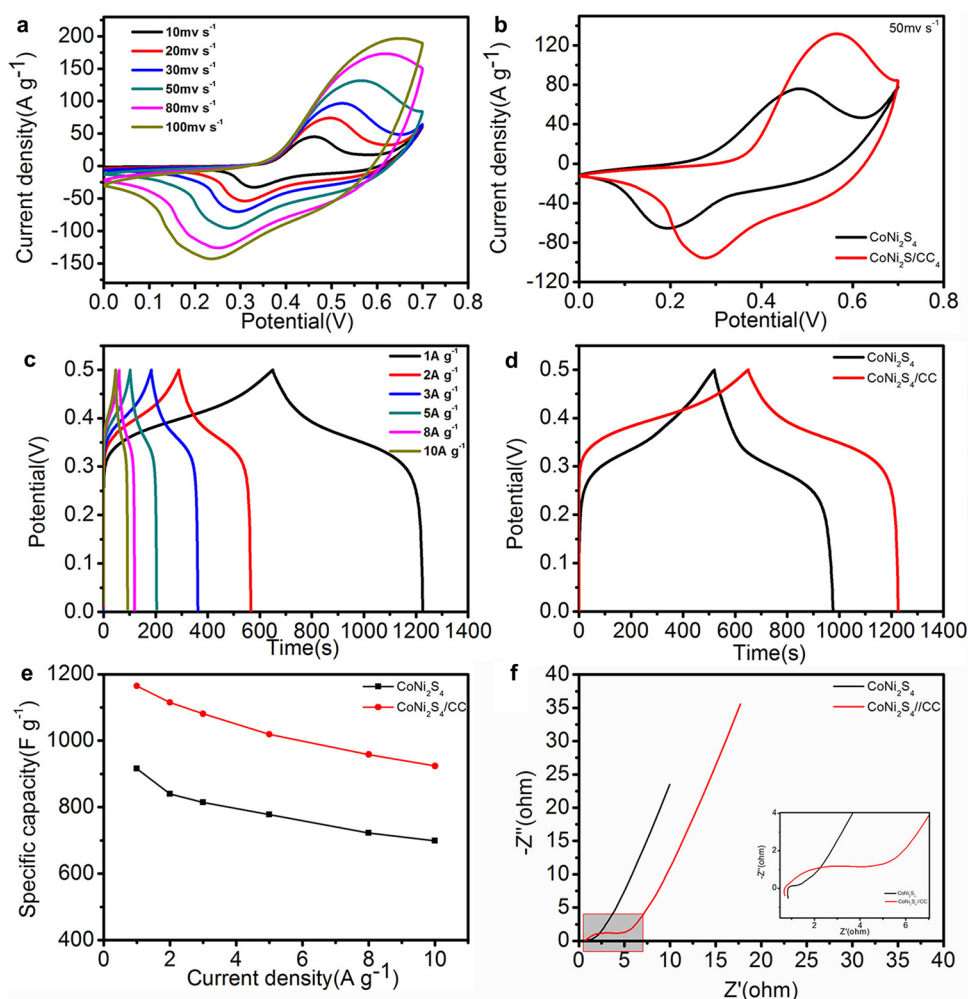


Fig. 3 SEM images of **a** bare CC; **b** CoNi_2S_4 loaded on carbon fiber cloth; **c** the pure CoNi_2S_4 samples at different magnifications; **d** HRTEM images of the $\text{CoNi}_2\text{S}_4/\text{CC}$ sample

Fig. 4 Electrochemical performance of CoNi_2S_4 as a supercapacitor in a three-electrode system: **a** CV curves of the $\text{CoNi}_2\text{S}_4/\text{CC}$ sample at various scan rates; **b** CV curves of the $\text{CoNi}_2\text{S}_4/\text{CC}$ and the pure CoNi_2S_4 samples at a scan rate of 50 mV s^{-1} ; **c** GCD curves of the $\text{CoNi}_2\text{S}_4/\text{CC}$ at various current densities; **d** GCD curves of the $\text{CoNi}_2\text{S}_4/\text{CC}$ and the pure CoNi_2S_4 samples at a current density of 1 A g^{-1} ; **e** comparison of specific capacitance; and **f** EIS Nyquist plots of the $\text{CoNi}_2\text{S}_4/\text{CC}$ and the pure CoNi_2S_4 samples



The GCD curves of both $\text{CoNi}_2\text{S}_4/\text{CC}$ electrode and pure CoNi_2S_4 electrode were performed at the current densities of 1, 2, 3, 5, 8 and 10 A g^{-1} and displayed in Fig. 4c, d. Figure 4c revealed the GCD measurements of the $\text{CoNi}_2\text{S}_4/\text{CC}$ electrode in the potential window of 0–0.5 V. The GCD curves clearly show distinct voltage plateaus, which is caused by the Faraday oxidation–reduction reaction during charging and discharging [31]. The two voltage plateaus are consistent with the redox peaks obtained from the CV analysis. The nonlinear shapes of these charge–discharge curves are similar and shown their ideal pseudocapacitive behaviors and Faraday reversible redox reaction between $\text{CoNi}_2\text{S}_4/\text{CC}$ and KOH electrolyte [30]. It is a typical pseudocapacitive property of transition metal compounds which was derived from the absorption/desorption of the electrolyte ions at the electrode–electrolyte interface [2, 31]. Figure 4d reveals the direct GCD measurements comparison of the $\text{CoNi}_2\text{S}_4/\text{CC}$ electrode and pure CoNi_2S_4 electrode collected at 1 A g^{-1} .

As expected, the discharge time of the $\text{CoNi}_2\text{S}_4/\text{CC}$ electrode is longer, which suggests that the charge stored in $\text{CoNi}_2\text{S}_4/\text{CC}$ electrode is larger than that in pure CoNi_2S_4 electrode.

The calculated specific capacitances of $\text{CoNi}_2\text{S}_4/\text{CC}$ electrode and pure CoNi_2S_4 electrode are displayed in Fig. 4e. The specific capacitance of $\text{CoNi}_2\text{S}_4/\text{CC}$ electrode can be calculated to be 1165, 1114.8, 1080.6, 1019, 958.4 and 924 F g^{-1} at 1, 2, 3, 5, 8, and 10 A g^{-1} and its rate performance was 79.3%. In addition, as can be observed from Fig. 4e, the specific capacitances of $\text{CoNi}_2\text{S}_4/\text{CC}$ electrode decay gradually in pace with the increase of current density. This phenomenon can be interpreted by the fact that when the current density of charge/discharge is lower, ions not only have higher diffusion efficiency in the electrolyte, but also have higher migration efficiency in the electrode region [41]. When the current density of charge/discharge is higher, the migration and diffusion of electrolyte ions are limited due to diffusion effects [2, 32]. When the current density is the same, the specific capacitances of the pure CoNi_2S_4 electrodes are lower than the $\text{CoNi}_2\text{S}_4/\text{CC}$ electrode. While the pure CoNi_2S_4 electrode exhibits 916, 840, 814, 778, 722

and 699 F g^{-1} at 1, 2, 3, 5, 8, and 10 A g^{-1} , respectively, and its rate performance is 76.3%, which is due to the insufficient utilization of electrochemical active material. As can be observed, the capacity retention rate of the $\text{CoNi}_2\text{S}_4/\text{CC}$ electrode is higher than pure CoNi_2S_4 electrode. In order to study the electron transport characteristics of $\text{CoNi}_2\text{S}_4/\text{CC}$ electrode and pure CoNi_2S_4 electrode during the Faradic reactions, the EIS analysis was applied within the range of 0.01 Hz–100 kHz with the amplitude of 5 mV at an open circuit potential. As revealed in Nyquist plots (Fig. 4f), the curves include the linear part of the low frequency range and the semi-circle part of the high frequency range. In the high frequency range, the real axis intercept between the semicircle and the X coordinate represents internal resistance (R_s), which consists of the resistance of the active substance, the ionic resistance and the contact resistance [3, 4]. Obviously, the R_s of the $\text{CoNi}_2\text{S}_4/\text{CC}$ and CoNi_2S_4 electrodes are 0.70 and 0.85Ω , respectively. As comparable to the $\text{CoNi}_2\text{S}_4/\text{CC}$ electrode, the pure CoNi_2S_4 electrode has larger interfacial charge transfer resistance. All electrodes exhibit a similar semicircular arc shape in the high frequency range, and the size of the semicircle represents the size of the electrode/electrolyte interface charge-transfer resistance (R_{ct}) [3, 4]. The slope of the line at the low frequency (Warburg-type line) represents the Warburg impedance (Z_w) associated with ion diffusion [3, 30]. As shown in Nyquist plots, the slope difference between the two lines is very small. The line at the low frequency is close to Y-axis, which indicates that ions and electrolytes diffuse effectively in the whole system, resulting in lower diffusion resistance of the $\text{CoNi}_2\text{S}_4/\text{CC}$ and CoNi_2S_4 electrodes.

In order to better assess the feasibility of the $\text{CoNi}_2\text{S}_4/\text{CC}$ electrode, the $\text{CoNi}_2\text{S}_4/\text{CC}/\text{r-GO}$ ASC device was fabricated and measured by using the $\text{CoNi}_2\text{S}_4/\text{CC}$ sample and r-GO as the positive electrode and negative electrode in 2 M KOH electrolyte, respectively. The specific capacitance of r-GO material at 1 A g^{-1} is 165 F g^{-1} and the capacitance degradation is extremely small after 10,000 cycles. Figure 5a displays the CV curves of r-GO and the $\text{CoNi}_2\text{S}_4/\text{CC}$ electrodes within the voltage windows range of 1.0–0 V and 0–0.7 V at 50 mV s^{-1} , respectively. In addition, the optimal weight ratio between the $\text{CoNi}_2\text{S}_4/\text{CC}$ electrode and the r-GO electrode is about 1:3.1 according to the Eq. (2). According to the CV measurements exhibits in Fig. 5a, the maximum operation potential window of the $\text{CoNi}_2\text{S}_4/\text{CC}/\text{r-GO}$ ASC device can be extended up to 1.6 V. Even at 100 mV s^{-1} , the curve does not show obvious polarization, which indicates that the battery voltage is reasonable. It can be seen from Fig. 5b that the CV curves of the ASC device have only slight deviation with scanning rate of 10–100 mV s^{-1} and the potential window from 0 to 0.7 V, which indicates that this device has excellent reversibility of charge-storage. In order to evaluate the charging capacity more intuitively, GCD curves of the ASC device

under different current densities were tested, as illustrated in Fig. 5c. As shown in Fig. 5d, the specific capacities of the $\text{CoNi}_2\text{S}_4/\text{CC}/\text{r-GO}$ ASC device is calculated to be 93.31, 85.75, 80.25, 72.03, 65.45, and 60.75 F g^{-1} at 1, 2, 3, 5, 8, and 10 A g^{-1} , respectively, according to Eq. (1). As displayed in Fig. 5e, an equivalent circuit was used to fit the curves using the ZView software. The EIS curves are composed of semicircles at a high-frequency range which are related to the charge-transfer resistance at the electrolyte–electrode interface and a straight sloping line at the low-frequency range [42]. In the high frequency range, the real axis intercept represents internal resistance (R_s), caused by the contact resistance of interface between active material and current collector, and the intrinsic resistance from the electrode and electrolyte [3]. The R_s of the assembled devices is 1.354Ω , which implies that the interface charge transfer resistance is smaller. The semicircle at high frequency corresponds to the interface charge-transfer resistance (R_{ct}), caused by the faradic reactions ascribed to the conductivity of active materials [3]. The larger the diameter of the semicircle, the higher the impedance. In addition, the line at the low frequency is close to Y-axis, which indicates that ions and electrolytes diffuse effectively in the whole system, resulting in lower diffusion resistance of the device. Additionally, cyclic performance is also one of the important indicators for the practical application of supercapacitor electrode materials [43, 44]. It is worth noting that after 10,000 cycle numbers, this device retained approximately 87.1% initial capacitance at 10 A g^{-1} , which indicates its excellent cycling stability. One of the important reasons for capacitance decay in the cycling process is that the low spalling of active substances on the electrodes.

The power density (P) and energy density (E) are the important indicators of supercapacitors, which can be calculated from Eqs. (3) and (4) according to the GCD measurements (Fig. 5c) and the results were displayed in Fig. 6. The ASC device achieved the maximum energy density of 33.2 Wh kg^{-1} at 800 W kg^{-1} . Even when the power density was as high as 8000 W kg^{-1} , the energy density still retained 21.6 Wh kg^{-1} . The obtained energy densities and power densities of this $\text{CoNi}_2\text{S}_4/\text{CC}/\text{r-GO}$ device was competitive in current researches, such as CoNi_2S_4 NS//AC (33.9 Wh kg^{-1} at 409 W kg^{-1}) [32], NiCo_2S_4 nanoparticles//AC (28.3 Wh kg^{-1} at 245 W kg^{-1}) [45], Ni-Co-sulfide NW AS//AC (25 Wh kg^{-1} at 447 W kg^{-1}) [46], NiS HNP//AC (11.6 Wh kg^{-1} at 187.5 W kg^{-1}) [47], $\text{NiCo}_2\text{O}_4/\text{CuCo}_2\text{O}_4$ //AC (15 Wh kg^{-1} at 814 W kg^{-1}) [48] and nickel–cobalt oxide//AC (10.8 Wh kg^{-1} at 474.4 W kg^{-1}) [49].

Fig. 5 The electrochemical measurements of the resultant $\text{CoNi}_2\text{S}_4/\text{CC}/\text{r-GO}$. **a** CV of the resultant $\text{CoNi}_2\text{S}_4/\text{CC}$ and r-GO at 50 mV s^{-1} ; **b** CV curves of the device at different current densities; **c** GCD curves of the ASC device; **d** the specific capacitance at various current densities; **e** EIS Nyquist plots of the device; **f** Cycling performance of the device at 10 A g^{-1} for 10,000 cycles

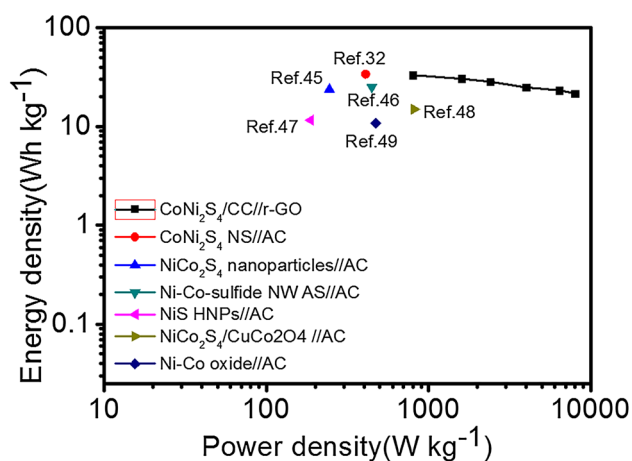
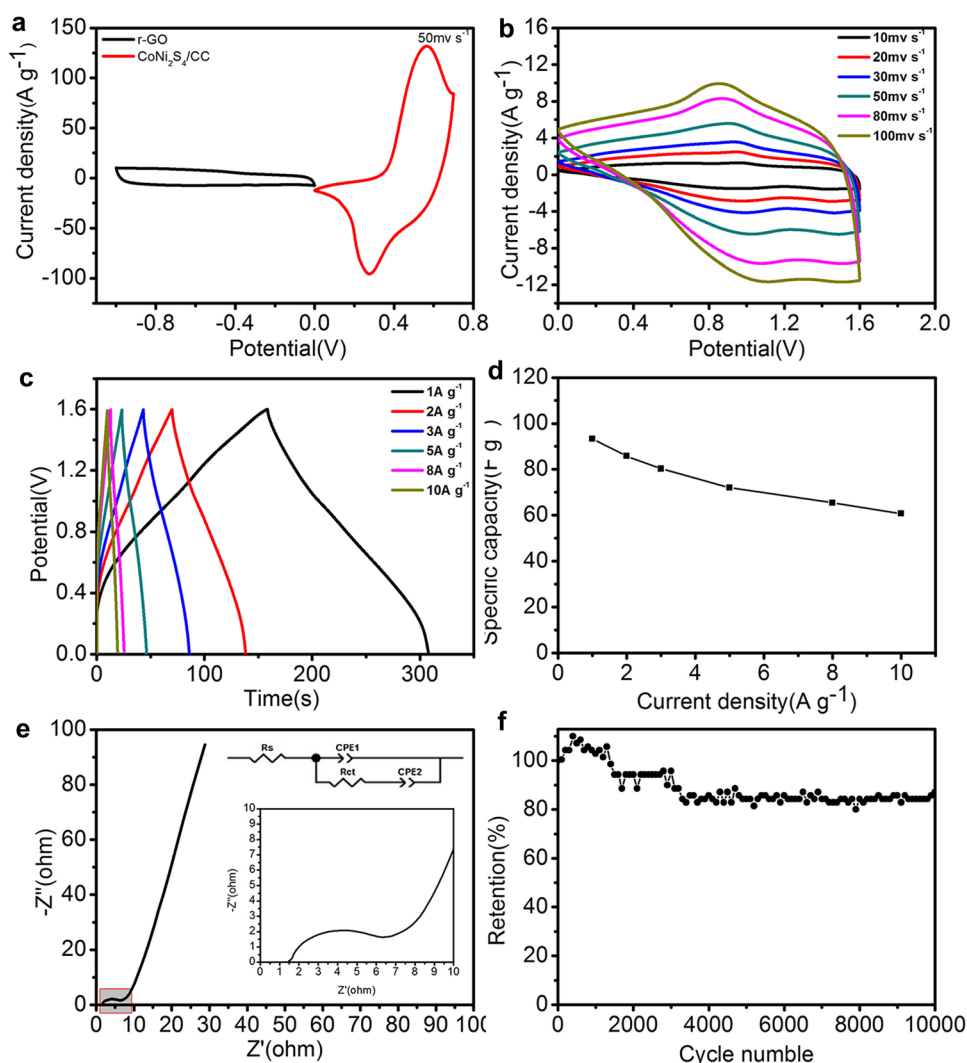


Fig. 6 The Ragone plots of the ASC device

4 Conclusion

In summary, a facile one-step hydrothermal route for application has been used to directly synthesize CoNi_2S_4 nanoparticles on CC. The CC substrates can increase the contribution of surface capacitance to the total capacitance, accelerate the transport of ions, and improve the utilization rate of CoNi_2S_4 , thereby achieving better rate performance. The resultant CoNi_2S_4 sample exhibits a high specific capacitance of 1165 F g^{-1} at 1 A g^{-1} and an outstanding rate capability of 79.3% at 10 A g^{-1} . Moreover, the maximum energy density of the $\text{CoNi}_2\text{S}_4/\text{CC}/\text{r-GO}$ ASC device can reach up to 33.18 Wh kg^{-1} at specific power of 800 W kg^{-1} , and still remained 21.6 Wh kg^{-1} at 8000 W kg^{-1} . Hence, these results suggested that the constructed $\text{CoNi}_2\text{S}_4/\text{CC}/\text{r-GO}$ ASC device exhibited an outstanding electrochemical characteristic.

Acknowledgments The authors would like to acknowledge the support by the Fundamental Research Funds for the Central Universities (No. 2019XKQYMS01).

References

1. Y. Zhao, X. Zhang, J. He et al., Morphology controlled synthesis of nickel cobalt oxide for supercapacitor application with enhanced cycling stability. *Electrochim. Acta* **174**, 51–56 (2015)
2. F. Huang, Y. Sui, F. Wei et al., Ni₃S₄ supported on carbon cloth for high-performance flexible all-solid-state asymmetric supercapacitors. *J. Mater. Sci. Mater. Electron.* **29**(3), 2525–2536 (2018)
3. S. Gao, Y. Sui, F. Wei et al., Dandelion-like nickel/cobalt metal-organic framework based electrode materials for high performance supercapacitors. *J. Colloid Interface Sci.* **531**, 83–90 (2018)
4. S. Gao, Y. Sui, F. Wei et al., Facile synthesis of cuboid Ni-MOF for high-performance supercapacitors. *J. Mater. Sci.* **53**(9), 6807–6818 (2018)
5. F. Chen, H. Wang, S. Ji et al., A 3D petal-like Ni₃S₂/CoNi₂S₄ hybrid grown on Ni foam as a binder-free electrode for energy storage. *Sustain. Energy Fuels* **2**(8), 1791–1798 (2018)
6. Z. Chen, Z. Li, X. Ma et al., A new DMF-derived ionic liquid with ultra-high conductivity for high-capacitance electrolyte in electric double-layer capacitor. *Electrochim. Acta* **319**, 843–848 (2019)
7. X. Zhang, X. Wang, L. Jiang et al., Effect of aqueous electrolytes on the electrochemical behaviors of supercapacitors based on hierarchically porous carbons. *J. Power Sources* **216**, 290–296 (2012)
8. S. Chen, K. Wen, J. Fan et al., Progress and future prospects of high-voltage and high-safety electrolytes in advanced lithium batteries: from liquid to solid electrolytes. *J. Mater. Chem. A* **6**(25), 11631–11663 (2018)
9. P. Perret, Z. Khani, T. Brousse et al., Carbon/PbO₂ asymmetric electrochemical capacitor based on methanesulfonic acid electrolyte. *Electrochim. Acta* **56**(24), 8122–8128 (2011)
10. X. Xu, X. Tian, X. Li et al., Structural and chemical synergistic effect of NiCo₂S₄ nanoparticles and carbon cloth for high performance binder-free asymmetric supercapacitors. *Appl. Surf. Sci.* **465**, 635–642 (2019)
11. X. Yu, M. Wang, A. Gagnoud et al., Formation of highly porous NiCo₂S₄ discs with enhanced pseudocapacitive properties through sequential ion-exchange. *Mater. Des.* **145**, 135–143 (2018)
12. S.J. Patil, D. Lee, Scalable and ascendant synthesis of carbon cloth coated hierarchical core-shell CoMoS@Co(OH)₂ for flexible and high-performance supercapacitors. *J. Mater. Chem. A* **6**(20), 9592–9603 (2018)
13. Y. Zhu, F. Wang, H. Zhang et al., PPy@NiCo₂S₄ nanosheets anchored on graphite foam with bicontinuous conductive network for high-areal capacitance and high-rate electrodes. *J. Alloys Compd.* **747**, 276–282 (2018)
14. Y. Zheng, J. Xu, X. Yang et al., Decoration NiCo₂S₄ nanoflakes onto Ppy nanotubes as core-shell heterostructure material for high-performance asymmetric supercapacitor. *Chem. Eng. J.* **333**, 111–121 (2018)
15. W. Du, Z. Zhu, Y. Wang et al., One-step synthesis of CoNi₂S₄ nanoparticles for supercapacitor electrodes. *RSC Adv.* **4**(14), 6998–7002 (2014)
16. J. Pu, F. Cui, S. Chu et al., Preparation and electrochemical characterization of hollow hexagonal NiCo₂S₄ nanoplates as pseudocapacitor materials. *ACS Sustain. Chem. Eng.* **2**(4), 809–815 (2014)
17. L. Mei, T. Yang, C. Xu et al., Hierarchical mushroom-like CoNi₂S₄ arrays as a novel electrode material for supercapacitors. *Nano Energy* **3**, 36–45 (2014)
18. Q. Hu, W. Ma, G. Liang et al., Anion-exchange reaction synthesized CoNi₂S₄ nanowires for superior electrochemical performances. *RSC Adv.* **5**(103), 84974–84979 (2015)
19. H. Wan, J. Jiang, J. Yu et al., NiCo₂S₄ porous nanotubes synthesis via sacrificial templates: high-performance electrode materials of supercapacitors. *CrystEngComm* **15**(38), 7649–7651 (2013)
20. L.G. Beka, X. Li, W. Liu, In situ grown cockscomb flower-like nanostructure of NiCo₂S₄ as high performance supercapacitors. *J. Mater. Sci. Mater. Electron.* **27**(10), 10894–10904 (2016)
21. J. Li, Q. Zhuang, P. Xu et al., Three-dimensional lily-like CoNi₂S₄ as an advanced bifunctional electrocatalyst for hydrogen and oxygen evolution reaction. *Chin. J. Catal.* **39**(8), 1403–1410 (2018)
22. Z. Wu, X. Pu, X. Ji et al., High energy density asymmetric supercapacitors from mesoporous NiCo₂S₄ nanosheets. *Electrochim. Acta* **174**, 238–245 (2015)
23. T. Wang, B. Zhao, H. Jiang et al., Electro-deposition of CoNi₂S₄ flower-like nanosheets on 3D hierarchically porous nickel skeletons with high electrochemical capacitive performance. *J. Mater. Chem. A* **3**(45), 23035–23041 (2015)
24. L. Yu, L. Zhang, H.B. Wu et al., Formation of Ni_xCo_{3-x}S₄ hollow nanoprisms with enhanced pseudocapacitive properties. *Angew. Chem. Int. Ed.* **53**(14), 3711–3714 (2014)
25. W. He, C. Wang, H. Li et al., Ultrathin and porous Ni₃S₂/CoNi₂S₄ 3D-network structure for superhigh energy density asymmetric supercapacitors. *Adv. Energy Mater.* **7**, 170098321 (2017)
26. F. Gao, B. Xu, Q. Wang et al., Potentiostatic deposition of CoNi₂S₄ nanosheet arrays on nickel foam: effect of deposition time on the morphology and pseudocapacitive performance. *J. Mater. Sci.* **51**(23), 10641–10651 (2016)
27. R. Ding, M. Zhang, Y. Yao et al., Crystalline NiCo₂S₄ nanotube array coated with amorphous NiCo_xS_y for supercapacitor electrodes. *J. Colloid Interface Sci.* **467**, 140–147 (2016)
28. W. Chen, C. Xia, H.N. Alshareef, One-step electrodeposited nickel cobalt sulfide nanosheet arrays for high-performance asymmetric supercapacitors. *ACS Nano* **8**(9), 9531–9541 (2014)
29. L. Hao, L. Shen, J. Wang et al., Hollow NiCo₂S₄ nanotube arrays grown on carbon textile as a self-supported electrode for asymmetric supercapacitors. *RSC Adv.* **6**(12), 9950–9957 (2016)
30. F. Huang, A. Yan, Y. Sui et al., One-step hydrothermal synthesis of Ni₃S₄@MoS₂ nanosheet on carbon fiber paper as a binder-free anode for supercapacitor. *J. Mater. Sci. Mater. Electron.* **28**(17), 12747–12754 (2017)
31. J.A. Rajesh, J. Park, H.V.Q. Vu et al., Rambutan-like cobalt nickel sulfide (CoNi₂S₄) hierarchitectured for high-performance symmetric aqueous supercapacitors. *J. Ind. Eng. Chem.* **63**, 73–83 (2018)
32. W. Hu, R. Chen, W. Xie et al., CoNi₂S₄ nanosheet arrays supported on nickel foams with ultrahigh capacitance for aqueous asymmetric supercapacitor applications. *ACS Appl. Mater. Int.* **6**(21), 19318–19326 (2014)
33. Z. Li, D. Zhao, C. Xu et al., Reduced CoNi₂S₄ nanosheets with enhanced conductivity for high-performance supercapacitors. *Electrochim. Acta* **278**, 33–41 (2018)
34. E. Hu, J. Ning, D. Zhao et al., A room-temperature postsynthetic ligand exchange strategy to construct mesoporous Fe-doped CoP hollow triangle plate arrays for efficient electrocatalytic water splitting. *Small* **14**, 170423314 (2018)
35. S.J. Patil, J.H. Kim, D.W. Lee, Self-assembled Ni₃S₂/CoNi₂S₄ nanoarrays for ultra high-performance supercapacitor. *Chem. Eng. J.* **322**, 498–509 (2017)
36. Z. Ai, Z. Hu, Y. Liu et al., Novel 3D flower-like CoNi₂S₄/carbon nanotube composites as high-performance electrode materials for supercapacitors. *New J. Chem.* **40**(1), 340–347 (2016)
37. F. Lu, M. Zhou, W. Li et al., Engineering sulfur vacancies and impurities in NiCo₂S₄ nanostructures toward optimal supercapacitive performance. *Nano Energy* **26**, 313–323 (2016)

38. G. Li, M. Liu, M. Wu et al., MOF-derived self-sacrificing route to hollow NiS₂/ZnS nanospheres for high performance supercapacitors. *RSC Adv.* **6**(105), 103517–103522 (2016)
39. C. Wu, J. Cai, Q. Zhang et al., Hierarchical mesoporous zinc-nickel-cobalt ternary oxide nanowire arrays on nickel foam as high-performance electrodes for supercapacitors. *ACS Appl. Mater. Int.* **7**(48), 26512–26521 (2015)
40. W. Xiong, X. Hu, X. Wu et al., A flexible fiber-shaped supercapacitor utilizing hierarchical NiCo₂O₄@polypyrrole core-shell nanowires on hemp-derived carbon. *J. Mater. Chem. A* **3**(33), 17209–17216 (2015)
41. F. Huang, R. Meng, Y. Sui et al., One-step hydrothermal synthesis of a CoS₂@MoS₂ nanocomposite for high-performance supercapacitors. *J. Alloys Compd.* **742**, 844–851 (2018)
42. G. Ali, M. Islam, H. Jung et al., Probing the sodium insertion/extraction mechanism in a layered NaVO₃ anode material. *ACS Appl. Mater. Int.* **10**(22), 18717–18725 (2018)
43. W. Lu, Z. Yuan, C. Xu et al., Construction of mesoporous Cu-doped Co₉S₈ rectangular nanotube arrays for high energy density all-solid-state asymmetric supercapacitors. *J. Mater. Chem. A* **7**(10), 5333–5343 (2019)
44. E. Hu, X. Yu, F. Chen et al., Graphene layers-wrapped Fe/Fe₅C₂ nanoparticles supported on n-doped graphene nanosheets for highly efficient oxygen reduction. *Adv. Energy Mater.* **8**, 17024769 (2018)
45. Y. Zhu, Z. Wu, M. Jing et al., Mesoporous NiCo₂S₄ nanoparticles as high-performance electrode materials for supercapacitors. *J. Power Sources* **273**, 584–590 (2015)
46. Y. Li, L. Cao, L. Qiao et al., Ni-Co sulfide nanowires on nickel foam with ultrahigh capacitance for asymmetric supercapacitors. *J. Mater. Chem. A* **2**(18), 6540–6548 (2014)
47. Z. Li, X. Yu, A. Gu et al., Anion exchange strategy to synthesis of porous NiS hexagonal nanoplates for supercapacitors. *Nanotechnology* **28**, 0654066 (2017)
48. X. Yang, H. Sun, P. Zan et al., Growth of vertically aligned Co₃S₄/CoMo₂S₄ ultrathin nanosheets on reduced graphene oxide as a high-performance supercapacitor electrode. *J. Mater. Chem. A* **4**(48), 18857–18867 (2016)
49. L. Kang, S. Sun, L. Kong et al., Investigating metal-organic framework as a new pseudo-capacitive material for supercapacitors. *Chin. Chem. Lett.* **25**(6), 957–961 (2014)

Publisher's Note Springer Nature remains neutral with regard to jurisdictional claims in published maps and institutional affiliations.